



AFRL-OSR-VA-TR-2014-0119

INFORMATION THEORETIC STUDIES AND ASSESMENTS OF SPACE-OBJECT IDENTIFICATION

Sudhakar Prasad
UNIVERSITY OF NEW MEXICO

03/24/2014
Final Report

DISTRIBUTION A: Distribution approved for public release.

Air Force Research Laboratory
AF Office Of Scientific Research (AFOSR)/ RTB
Arlington, Virginia 22203
Air Force Materiel Command

REPORT DOCUMENTATION PAGE				<i>Form Approved</i> OMB No. 0704-0188	
<small>Public reporting burden for this collection of information is estimated to average 1 hour per response, including the time for reviewing instructions, searching existing data sources, gathering and maintaining the data needed, and completing and reviewing this collection of information. Send comments regarding this burden estimate or any other aspect of this collection of information, including suggestions for reducing this burden to Department of Defense, Washington Headquarters Services, Directorate for Information Operations and Reports (0704-0188), 1215 Jefferson Davis Highway, Suite 1204, Arlington, VA 22202-4302. Respondents should be aware that notwithstanding any other provision of law, no person shall be subject to any penalty for failing to comply with a collection of information if it does not display a currently valid OMB control number. PLEASE DO NOT RETURN YOUR FORM TO THE ABOVE ADDRESS.</small>					
1. REPORT DATE (DD-MM-YYYY)		2. REPORT TYPE		3. DATES COVERED (From - To)	
4. TITLE AND SUBTITLE				5a. CONTRACT NUMBER	
				5b. GRANT NUMBER	
				5c. PROGRAM ELEMENT NUMBER	
6. AUTHOR(S)				5d. PROJECT NUMBER	
				5e. TASK NUMBER	
				5f. WORK UNIT NUMBER	
7. PERFORMING ORGANIZATION NAME(S) AND ADDRESS(ES)				8. PERFORMING ORGANIZATION REPORT NUMBER	
9. SPONSORING / MONITORING AGENCY NAME(S) AND ADDRESS(ES)				10. SPONSOR/MONITOR'S ACRONYM(S)	
				11. SPONSOR/MONITOR'S REPORT NUMBER(S)	
12. DISTRIBUTION / AVAILABILITY STATEMENT					
13. SUPPLEMENTARY NOTES					
14. ABSTRACT					
15. SUBJECT TERMS					
16. SECURITY CLASSIFICATION OF:			17. LIMITATION OF ABSTRACT	18. NUMBER OF PAGES	19a. NAME OF RESPONSIBLE PERSON
a. REPORT	b. ABSTRACT	c. THIS PAGE			19b. TELEPHONE NUMBER (include area code)

Final Report

Information Theoretic Studies and Assessment of Space Object Identification

June 1, 2009 - November 30, 2013

Prof. S. Prasad, PI

March 21, 2014

Grant No. FA9550-09-1-0495

Abstract

This document represents the final report on the various scientific activities and accomplishments relating to Grant No. FA9550-09-1-0495 over its period of performance, June 1, 2009 - November 30, 2013. The project had the following three overarching technical objectives:

1. Numerical evaluations of multivariate statistical entropies and information for imaging problems
2. Information-theoretic assessment of PSF errors and their impact on image quality in an SOI imaging system
3. Optimal choice of regularization functional in image reconstruction

The following is a list of the most important technical accomplishments of the project:

- A new relation between two seemingly different metrics of information - mutual information (MI) and estimation theoretic Fisher information (FI) in the high-SNR limit, for arbitrary input and channel probability distributions;
- New numerically efficient, tight upper and lower bounds on successfully transmitted statistical information, namely MI, in the estimation of one or more features of a target based on image data;
- Improved approaches for an exact numerical, Monte-Carlo-sampling based computation of MI and comparison with our tight upper bounds for some problems;

- Bayesian approaches to the problem of optimal selection of regularizer and its strength based on data themselves;
- The development of a tight, variational upper bound on the minimum Bayesian estimation error, the so called minimum mean-squared error (MMSE), that is tighter than and superior to several more widely known lower bounds on the MMSE, such as the Ziv-Zakai and Weiss-Weinstein bounds;
- An improved lower bound on the MMSE that is tighter than the standard Ziv-Zakai bound and is based on the minimum probability of error (MPE) of a related M -ary hypothesis testing based Bayesian inference;
- A computational-imaging approach to encoding the field depth of a target using the rotation of a point-spread function based on the orbital angular momentum (OAM) states of light - this can be employed to track, fully in 3D, unresolved space objects, such as orbital debris that could pose a potential threat to space assets; and
- A full Bayesian error analyses of the prospects of 3D localization and super-resolution of unresolved sources beyond the standard diffraction limit of an imaging system.

These technical accomplishments have resulted in a total of 19 publications, 11 presentations (6 invited, 5 contributed), and 1 US patent application.

1 Summary of Overall Project Accomplishments

The three originally proposed objectives of the effort were largely achieved over the project duration. In this report we provide only a summary description of the project accomplishments, leaving the many technical details of a fuller description to the project-supported publications that are cited at appropriate places below and are publicly accessible.

An overarching objective of the effort was to construct useful statistical formalisms in which one can analyze the identification, characterization, and reconstruction of space objects in the combined spatial-spectral domain. The formalisms we developed during the project are based on Bayesian error analysis on the one hand and statistical information on the other, and exploit new insights into their mutual relationship based on improved versions of certain inequalities such as the Fano bound.

Our technical accomplishments may be summarized as follows:

1.1 A New Relation between Estimation-Theoretic Fisher Information and Mutual Information

An important task was to unify estimation theoretic notions of information and noise performance based on Fisher information (FI) with concepts like mutual information, compressibility and complexity described by Shannon's statistical information. FI is a measure of local sensitivity of statistical data to a parameter that has to be estimated from the data. As such it involves a statistical average of a bilinear product of the first derivatives of the logarithm of the data probability distribution (PD) with respect to the parameters being estimated. By contrast, mutual information (MI), $I(X;Y)$, is the amount of statistical information about a parameter X that can be passed by a communication channel, or more generally by a measuring system, through its statistical output, Y , in the presence of noise and other system limitations. It is thus a global and Bayesian measure of information. A handful of relations are known between FI and MI, but only one previously known such relation has any physical content, namely the (negative) difference between MI and the statistical entropy, $H(X)$, of the input, the latter representing the maximum information that the system can transmit under ideal circumstances (i.e., no noise and other limitations) depends on the FI in the asymptotic limit of many repeated measurements, Y_1, Y_2, \dots [see, e.g., Kang and Sompolinsky, "Mutual information of population codes and distance measures in probability space," Phys. Rev. Lett., **86**, pp. 4958-4961 (2001)]. This is an expected result since in the asymptotic limit, the SNR becomes infinitely large, and all global information metrics become local.

The relation we have derived is a different one that applies for *any* number of measurements, $\mathbf{Y} \equiv \{Y_1, \dots, Y_M\}$, or of input parameters, $\mathbf{X} = \{X_1, \dots, X_P\}$. It is based on the observation that when the PD of \mathbf{X} is sufficiently narrow the *local* and *global* measures of information are expected to be in agreement. That this is indeed true is contained in the following expression we have derived that is valid to the second order in the width of the X -PDF:

$$I(\mathbf{X}; \mathbf{Y}) = \frac{1}{2} \int d\mathbf{x} P(\mathbf{x}) \sum_{j,k} \delta x_j \delta x_k J_{jk}(\mathbf{Y}|\mathbf{x}), \quad (1)$$

where $\delta x_i = x_i - \langle X_i \rangle$ denotes the linear deviation of x_i from its mean value, $\langle X_i \rangle$. For a single input parameter, X , this reduces to the following simple expression:

$$I(X; \mathbf{Y}) = \frac{1}{2} \int dx P(x) (x - \langle X \rangle)^2 J(\mathbf{Y}|x). \quad (2)$$

Unfortunately, this result does not seem to have a simple generalization for arbitrary widths of the input PD, for which global and local metrics of information must in general be quite different.

1.2 Certain Logarithmic Upper and Lower Bounds on Mutual Information

Computing the statistical entropy and associated MI requires the evaluation of statistical averages of logarithms of PDs and their ratios, as we have noted earlier. When many parameters and measurements are involved, these averages amount to high-dimensional integrals which require efficient numerical approaches like Monte-Carlo (MC) integration to evaluate to high accuracy. However, because of the logarithm inside the typical integrand, one must sample the high-dimensional configuration space of these variables efficiently over vast regions before the logarithm is sufficiently attenuated and begins to contribute negligibly in order to yield accurate results. It is important therefore to consider more accurate and efficient approaches to MC evaluations of MI.

We have developed useful upper and lower bounds to MI that altogether avoid integrating logarithms of PDs and their ratios. By writing $\ln[P(y|x)/P(y)] = (1/\alpha) \ln[P(y|x)/P(y)]^\alpha = -(1/\beta) \ln[P(y|x)/P(y)]^{-\beta}$, with $\alpha, \beta > 0$, and using the convexity of the logarithm in the equivalent MI expressions,

$$\begin{aligned} I(X; Y) &= -\frac{1}{\alpha} \int \int dx dy P(x, y) \ln[P(y|x)/P(y)]^\alpha \\ &= \frac{1}{\beta} \int \int dx dy P(x, y) \ln[P(y|x)/P(y)]^{-\beta}, \end{aligned} \quad (3)$$

we obtain the following logarithmic bounds on MI:

$$\begin{aligned} -\frac{1}{\beta} \ln \int \int dx dy P(x, y) \left[\frac{P(y|x)}{P(y)} \right]^{-\beta} \\ \leq I(X; Y) \leq \frac{1}{\alpha} \ln \int \int dx dy P(x, y) \left[\frac{P(y|x)}{P(y)} \right]^\alpha. \end{aligned} \quad (4)$$

These constitute a family of logarithmic bounds, which we refer to as α and β bounds, which get progressively tighter as α and β decrease from positive values to 0.

These bounds are already quite tight even for values of α, β of order 0.5 or less, as we show in Figure 1 for the case of the Poisson channel and negative-exponential statistics for X . Note that even for α, β equal to 1/2, the bounds are within 10% of the exact result. Indeed, by averaging the upper and lower bounds corresponding to the same value of α and β , we are likely to get within 1-2% of the exact result, obviating thus the need, in the exact MI expression, for numerically inefficient averaging of logarithms of PDFs that may become exceptionally small for high-dimensional spaces of input and data variables.

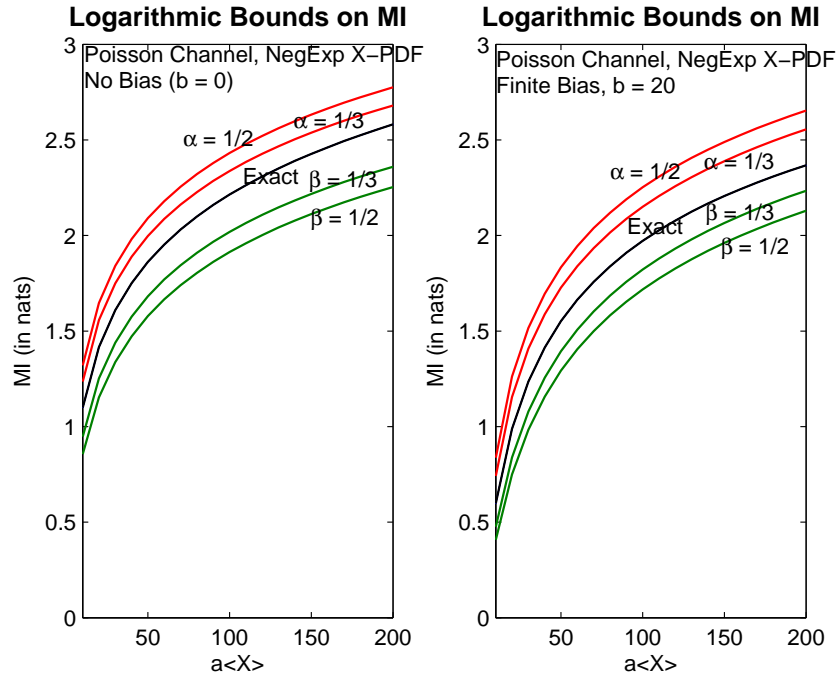


Figure 1: Exact MI and the logarithmic α and β bounds on it, for Poisson channel and negative exponential statistics for X . The conditional mean of the Poisson channel, given x , is $ax + b$, where a is the linear gain factor and b the bias of the channel. The mean value of X is $\langle X \rangle$.

1.3 Useful Bayesian Bounds on MI

In the vein of discovering further bounds that avoid the numerical inaccuracies of MC based computations of MI, such as Metropolis-Hastings and improved versions thereof, we turn to the fact that Bayesian metrics of performance can be quite useful in this respect. The two most popular Bayesian metrics are the MMSE and MPE, both of which relate to estimators that, respectively, are the mean and mode of the posterior PDF, namely $P(x|y)$. The expected value of the negative logarithm of the same posterior, or the equivocation entropy, is precisely the loss of statistical information, and hence the fact that the MI is related to MMSE and MPE is no serious surprise. It is this relationship and its many consequences for bounding MI in terms of these Bayesian metrics as well as the equivalence of MMSE and MPE to each other in the high SNR limit that we studied in detail under the grant effort.

1.3.1 A Generalized Fano Lower Bound on MI for a Continuous Source

The usual Fano inequality connecting the probability of error in estimating a source from its measurements to the equivocation entropy has been an excellent tool in relating Bayesian detection and estimation analysis to statistical information theory. It is however based on the discreteness of the sample space, \mathcal{X} , of the source variable, X , for which the following Fano bound is valid:

$$I(X; Y) \geq H(X) - H(P_e) - P_e \log_2(|\mathcal{X}| - 1) \geq H(X) - 1 - P_e \log_2 |\mathcal{X}|, \quad (5)$$

in which P_e is the MPE in predicting the value of a discrete random variable X from data Y .

We derived a version of the Fano bound that applies to a continuous source variable. If one defines an ϵ -error variable E_ϵ as

$$E_\epsilon = \begin{cases} 1 & \text{if } |\hat{X} - X| > \epsilon \\ 0 & \text{if } |\hat{X} - X| \leq \epsilon. \end{cases} \quad (6)$$

then the analog of inequality (5), as we have shown, becomes

$$I(X; \hat{X}) \geq h(X) - H(P_e) - (1 - P_e) \log 2\epsilon - P_e \frac{1}{2} \log(2\pi e \text{MMSE}_\epsilon), \quad (7)$$

where MMSE_ϵ is the (Bayesian) minimum MSE for the joint PDF defined only over the excluded region, $|\hat{X} - X| > \epsilon$. The practical usefulness of this result is unclear, since it involves the MMSE which even for the fully included X, \hat{X} region is usually very hard to compute. However, it may at the very least provide a useful formal tool to prove new theoretical relations between the Bayesian and information theoretic approaches for upper-bounding system performance.

1.3.2 Other Bayesian Bounds on MI

For a discrete source variable, X , the equivocation entropy $H(X|Y)$, which is simply $-\mathbb{E} \log P(X|Y)$, is clearly bounded below by $-\mathbb{E} \log P(x_{m_*}(Y)|Y)$, where $m_*(Y)$ is the MAP estimator, namely

$$m_*(Y) = \operatorname{argmax}_m \{P(x_m|Y)\}, \quad (8)$$

in which $\{x_1, \dots, x_M\}$ is the sample space of the source X . Since the logarithm is a concave function, it then follows that

$$H(X|Y) \geq -\ln \mathbb{E}_Y P(x_{m_*(Y)}|Y) = -\ln(1 - P_e^{(min)}), \quad (9)$$

where $P_e^{(min)}$ is the MPE. This is the so-called Feder-Merhav (FM) bound derived two decades ago. The FM bound is typically not sharp. In our work, we found a number of improvements on the FM bound that make it much tighter, as we show for certain generic problems we considered.

One tighter bound follows from writing

$$-\log P(X|Y) = -\log \max_m P(x_m|Y) - \log \left[P(X|Y) / \max_m P(x_m|Y) \right], \quad (10)$$

and then calculate its expectation. Performing this expectation in two steps, first over the posterior and then over the data Y , and then using the concavity of the logarithm on the RHS above, we may obtain the following lower bound on EE:

$$\begin{aligned} H(X|Y) &\geq -\log \mathbb{E}_Y \max_m P(x_m|Y) + \Delta \\ &= -\log(1 - P_e^{(min)}) + \Delta, \end{aligned} \quad (11)$$

where Δ denotes the expression

$$\Delta \stackrel{\text{def}}{=} -\log \mathbb{E}_Y \left[\frac{\sum_m P^2(x_m|Y)}{\max_m P(x_m|Y)} \right]. \quad (12)$$

By means of the Bayes theorem, $P(x_m|y) = P(y|x_m)p_m/P(y)$, we may express Δ as

$$\Delta = -\log \left[\sum_m \int dy \frac{p_m^2}{p_{m_*(y)}} \frac{P^2(y|x_m)}{P(y|x_{m_*(y)})} \right], \quad (13)$$

with the corresponding lower bound on EE via (11) being

$$\begin{aligned} H(\Theta|X) &\geq -\log(1 - P_e^{(min)}) \\ &\quad -\log \left[\sum_m \int dx \frac{p_m^2}{p_{m_*(x)}} \frac{P^2(x|\theta_m)}{P(x|\theta_{m_*(x)})} \right]. \end{aligned} \quad (14)$$

Subtracting the RHS of bound (14) from $H(X)$ yields the corresponding upper bound on MI.

If instead of (11), we write the exact equality

$$H(X|Y) = -\mathbb{E}_Y \log \max_m P(x_m|Y) + \Delta', \quad (15)$$

where Δ' is the difference

$$\Delta' = -\mathbb{E} \log \left[1 - \frac{\max_m P(x_m|Y) - P(X|Y)}{\max_m P(x_m|Y)} \right], \quad (16)$$

and then use the inequality $-\ln(1-u) \geq u$, valid for $0 \leq u < 1$, to upper-bound Δ' as

$$\Delta' \geq (\log e) \left[1 - \sum_m \int dy \frac{p_m^2}{p_{m^*}(y)} \frac{P^2(y|x_m)}{P(y|x_{m^*}(y))} \right]. \quad (17)$$

This bound involves the same integral as, but is looser than, (13). Since the first term on the RHS of expression (15) is lower-bounded by $-\log \mathbb{E}_X \max_m P(\theta_m|X)$, the EE is then lower-bounded as

$$\begin{aligned} H(\Theta|X) &\geq -\log(1 - P_e^{(min)}) \\ &\quad + (\log e) \left[1 - \sum_m \int dy \frac{p_m^2}{p_{m^*}(y)} \frac{P^2(y|x_m)}{P(y|x_{m^*}(y))} \right]. \end{aligned} \quad (18)$$

As before, subtracting the RHS of bound (18) from $H(X)$ yields the corresponding upper bound on MI.

The two lower bounds on $H(X|Y)$, (14) and (18), the latter tighter than the former, correspond to fairly tight upper bounds on MI and are denoted as SUB1 and SUB2, respectively, in Fig. 2. The looser Fano lower bound and the looser FM upper bound are also plotted and indicated as FLB and FM-UB, respectively, on the same figure which also displays the numerically exact MI. In this figure, the fractional MI, namely $I(X;Y)/H(X)$, refers to that for the joint angular position-chemical type feature, X , of a distant muzzle flash which is observed in a number of spectral bands by a array of single-pixel sensors (“light buckets”) mounted on a hemispherical surface like a soldier’s helmet as shown in Fig. 3.

More details of this work appear in a technical report prepared for a DARPA contract which partially supported the work.

A Useful Upper Bound for the Uniform Prior Denoting the difference of the posterior from the prior as $\delta P(X|Y) = P(X|Y) - P(X)$, we may express the sum in Eq. (12) as

$$\begin{aligned} \sum_m P^2(x_m|Y) &= \sum_m [P_m + \delta P(x_m|Y)]^2 \\ &= \sum_m [P_m^2 + \delta P^2(x_m|Y) + 2P_m \delta P(x_m|Y)]. \end{aligned} \quad (19)$$

For the uniform prior, the last term in expression (19) vanishes, since the posterior, like the prior, is a probability distribution that sums to 1, while the first term in the second expression there is simply $1/M$. In this case, the sum (19) thus differs from the corresponding sum over the prior probabilities, namely $1/M$, by terms that are of quadratic order in the deviations $\delta P(x_m|Y)$. This allows us to write the lower bound on equivocation as

$$\begin{aligned} H(X|Y) &= -\mathbb{E} \log P(X|Y) \\ &\geq -\log \mathbb{E} P(\Theta|Y) \\ &= -\log \mathbb{E}_Y \sum_m P^2(\theta_m|Y) \\ &= \log M - \log \left[1 + M \mathbb{E}_Y \sum_m \delta P^2(x_m|Y) \right], \end{aligned} \quad (20)$$

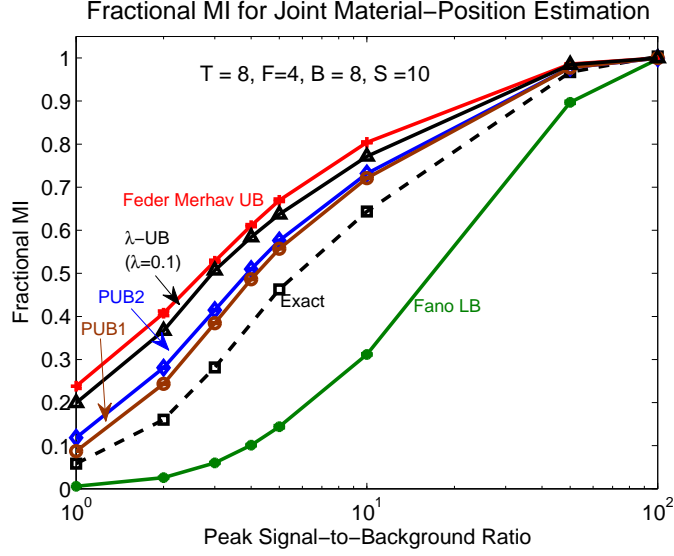


Figure 2: Fractional mutual information (fMI) vs. peak signal-to-background ratio (pSBR). Numerically exact results are shown via dashed line segments, while the Fano lower bound and the various upper bounds are shown via different marker symbols and colors. In all cases, the error in calculating the various results due to finiteness of sampling was smaller than the size of the marker symbol itself.

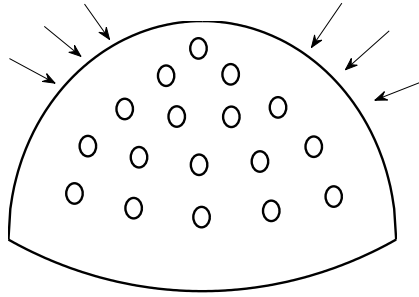


Figure 3: A schematic of the hemispherical mount for single-pixel multi-spectral sensors arranged regularly in rings on the mount. Arrows indicate possible angular directions of arrival of a distant muzzle flash.

so the MI is upper bounded as

$$I(X; Y) = H(X) - H(X|Y) \leq \log \left[1 + M \mathbb{E}_Y \sum_m \delta P^2(x_m|Y) \right]. \quad (21)$$

To obtain the first inequality in relation (20), we used the concavity of the logarithm, and then decomposed the full expectation into an expectation over the posterior followed by an expectation over the data before substituting expression (19) for the sum. The MI bound (21) is fairly tight, and interpolates between the $\log M$ value of MI in the high-discrimination regime where only one of the posterior probabilities is close to 1 and all the other $(M - 1)$ ones are close to 0, and the vanishing value of the MI in the low-discrimination regime where the correction contained in the sum on the RHS in the upper bound (21) tends to be small. While numerically inefficient to compute, in general, this bound has a very useful interpretation because of its analogy with the information capacity of an additive Gaussian channel for which the ratio of the mean squared deviations of the posterior from the prior and the uniform squared prior probability, $1/M^2$, serves as an effective SNR.

1.4 Optimal Choice of Regularization Functional in Image Reconstruction

In the first 3.5 years of the project, we studied in much detail the notion of accommodation by a regularizer defined as the degree of degradation of reconstruction as the regularization strength is increased beyond its optimal value. This is a measure of how well a regularizer continues to “fit” the reconstruction even when it dominates the fit-to-data term in the minimization functional. A good measure of the fit is the MSE, defined as the squared error in the reconstructed signal relative to the truth signal averaged over the Bayesian prior defined over the parameters that define the object class. By considering error in different attributes of the brightness distribution of the sources in the family, e.g., intensity gradients, rather than intensities themselves, one can in this approach rank the various regularizers according to their ability to accommodate different attributes such as edges, lines, and points.

We found by means of extensive simulation the superiority of Laplacian regularizer when compared to the Tikhonov, maximum-entropy (ME), and total-variation (TV) regularizers, for the object class that contains smooth Gaussian-shaped sources. Similar studies were extended to other classes of sources too, those containing rect functions and combinations of Gaussian and rect functions.

Most recently, our attention was focused on performing this analysis without the use of computer simulation so the reconstruction may be calculated analytically and the data statistics imposed essentially exactly on the MSE calculations. We have succeeded partially in this work by restricting attention to quadratic regularizers of form

$$\mathcal{R}(\underline{X}) = \frac{\lambda}{2} \underline{X}^T \mathbf{R} \underline{X}, \quad (22)$$

where \mathbf{R} is a real symmetric matrix with positive eigenvalues and \underline{X} is the vector of signal intensities at its pixels. By choosing three different regularizer matrices \mathbf{R} , we have been

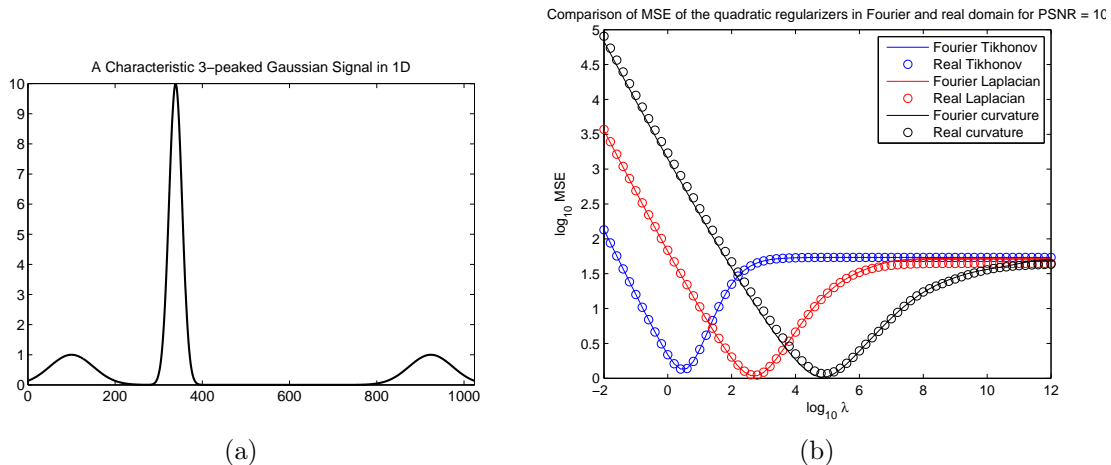


Figure 4: (a) The brightness distribution of a typical 1D signal consisting of three Gaussian shaped peaks. (b) The MSE vs. regularizer strength curves in a log-log plot for three different quadratic regularizers, as indicated in the legend on the plot. The PSNR value was fixed at 10 for this plot.

able to model reconstructions under Tikhonov, Laplacian, and curvature regularizations, and compare the curvatures of the corresponding $\log \text{MSE}$ vs. $\log \lambda$ curves at their minima as a measure of accommodation. As seen below in Fig. 4 (b), the curvature regularizer seems to do the best, the curvature of the corresponding MSE curve distinctly being the smallest for it. The class of signals we considered for these plots consists of three Gaussian shaped peaks in one dimension (1D), as shown in Fig. 4 (a). We have derived analytically an exact closed-form expression for the MSE, which we numerically evaluated either individually for each member of the object class or at once for the whole class by statistically averaging the analytical expression over the prior defining the class.

1.5 A Variational Upper Bound on the MMSE of Bayesian Estimation

A number of lower bounds on the MMSE, including Ziv-Zakai (ZZB) and Weiss-Weinstein (WWB) families of bounds, have been proposed and studied over the past 40 years. These lower bounds have reformulated the problem of Bayesian estimation in clever ways but they still have been difficult to calculate and apply to practical problems.

In order to overcome the problem of efficient computability of the MMSE and the corresponding MMSE estimator for general prior and channel PDFs, we turned out attention instead to simple upper bounds on the MMSE. We have derived one such upper bound that seems, in all cases we have studied so far, to be easy to compute and rather tight. Also, the celebrated lower bounds, ZZB and WWB, can be shown in some cases to be quite loose and thus of little value in accurately predicting error performance bounds, particularly for space imaging applications.

The minimum value of the MSE over the space of all possible estimators is attained by

the minimum MSE estimator (MMSEE), which is the posterior mean of the parameter X ,

$$\hat{X}_M(Y) = \mathbb{E}_{X|Y}(X) = \int x P(x|Y) dx. \quad (23)$$

The MSE of this estimator is the MMSE, \mathcal{E}_M , which can be simplified to the form

$$\begin{aligned} \mathcal{E}_M &= \mathbb{E}[\hat{X}_M(Y) - X]^2 \\ &= \sigma_X^2 - \sigma_{X_M}^2 \end{aligned} \quad (24)$$

involving the variances of the prior and the MMSEE, namely σ_X^2 and $\sigma_{X_M}^2$.

If $\hat{X}(Y)$ is another estimator of X , then by writing $\hat{X} - X = (\hat{X} - \hat{X}_M) + (\hat{X}_M - X)$, taking its mean squared value, and using Eqs. (23) and (24), we may express its MSE in the expanded form

$$\begin{aligned} \mathcal{E} &= \mathcal{E}_M + \mathbb{E}[\hat{X}(Y) - \hat{X}_M(Y)]^2 + 2\mathbb{E}[\hat{X}(Y) - \hat{X}_M(Y)][\hat{X}_M(Y) - X] \\ &= \mathcal{E}_M + \mathbb{E}[\hat{X}(Y) - \hat{X}_M(Y)]^2, \end{aligned} \quad (25)$$

which is obviously bounded below by the MMSE, \mathcal{E}_M . The second term in the second equality in (25) is the amount by which the MSE for an estimator must exceed the MMSE. By subtracting this term from both sides of the equality and noting that this term cannot be smaller than the square of the mean $\mathbb{E}[\hat{X}(Y) - \hat{X}_M(Y)]$, we have the following upper bound (UB) on the MMSE:

$$\begin{aligned} \mathcal{E}_M &\leq \mathcal{E} - \mathbb{E}^2[\hat{X}(Y) - \hat{X}_M(Y)] \\ &= \mathbb{E}[\hat{X}(Y) - X]^2 - \mathbb{E}^2[\hat{X}(Y) - X] \\ &= \mathbb{E}\{[\hat{X}(Y) - \mathbb{E}(\hat{X})] - [X - \mathbb{E}(X)]\}^2 \stackrel{\text{def}}{=} \mathcal{E}_{UB}, \end{aligned} \quad (26)$$

where the second line follows from the fact that the mean value of the MMSEE is simply the mean value of the prior, $\mathbb{E}_X(X)$. The third line represents a convenient way of combining the two terms in the second line and then regrouping them inside the square.

The rather simple upper bound (26) has the immediate benefit that it can be computed readily since, unlike the MMSE, it does not require any knowledge of the posterior PD, $P_{X|Y}$, the chief bane of any MMSE calculation. Furthermore, since according to Eq. (25) the MSE of any estimator differs from the MMSE in the quadratic order in the difference between the two estimators, a variational approach to estimate the MMSE by minimizing the UB (26) with respect to classes of estimators should yield excellent accuracy even when the estimator itself does not approximate the MMSEE as well. An analogous situation exists for the variational method for estimating the ground-state energy of a quantum mechanical energy problem. Note further that being smaller than the MSE, which is the first term in the second line of (26), the UB obtained from any trial estimator is already closer to the MMSE than its own MSE, and thus presumably furnishes a better starting point and a faster convergence to the MMSE.

1.5.1 MMSE Upper Bound for a Polynomial Family of Estimators

Consider first the simplest problem of a single parameter being estimated from a single observation and estimators belonging to the class of N th-order polynomials, *i.e.*,

$$\hat{X}_N(Y) = a_0 + \sum_{n=1}^N a_n Y^n. \quad (27)$$

We shall regard $\{a_n\}$ as variational parameters that need to be chosen to minimize the UB (26). Substituting the form (27) into the formula (26), we may express the UB as

$$\begin{aligned} \mathcal{E}_{UB} &= \mathbb{E} \left(\sum_{n=1}^N a_n \delta Y^n - \delta X \right)^2 \\ &= \underline{a}^T \mathbf{M} \underline{a} - 2 \underline{a}^T \underline{v} + \sigma_X^2, \end{aligned} \quad (28)$$

where \underline{a} denotes the vector $(a_1, \dots, a_N)^T$ (T : matrix transpose), \mathbf{M} an $N \times N$ matrix with elements, $M_{mn} = \mathbb{E}(\delta Y^m \delta Y^n)$, $m, n = 1, \dots, N$, and \underline{v} an $N \times 1$ vector of elements $\mathbb{E}(\delta X \delta Y^n)$, $n = 1, \dots, N$. The symbol δ preceding a variable denotes its deviation from its mean value, *e.g.*,

$$\delta Y^n \equiv Y^n - \mathbb{E}(Y^n). \quad (29)$$

Since the matrix \mathbf{M} is positive definite, the quadratic problem (28) has a single extremum that is its absolute minimum. Its location \underline{a}_* in the space of the parameter vector \underline{a} is determined by setting the gradient of the expression (28) with respect to the parameter vector \underline{a} equal to 0, namely $\mathbf{M} \underline{a}_* = \underline{v}$, or equivalently $\underline{a}_* = \mathbf{M}^{-1} \underline{v}$. The corresponding minimum value of the UB (28) then simplifies greatly to the final form

$$\mathcal{E}_{UB*} = \sigma_X^2 - \underline{v}^T \mathbf{M}^{-1} \underline{v}. \quad (30)$$

The minimum value of the UB (30) is both smaller than the prior variance, σ_X^2 , and lowered in general as the order of the polynomial, N , increases. To prove the latter assertion, we simply note that the class of $(N+1)$ th-order polynomials includes as a proper subset the class of N th order polynomials. Thus the minimum of the UB over the former class cannot be larger than the that over the latter class. A more rigorous mathematical proof may also be given based on Schur's inversion formula for the block-matrix form of a square matrix.

Curiously, the overall additive constant a_0 in the trial form (27) of the estimator is left undetermined. This is not a surprise since the UB form (28) is clearly insensitive to any overall additive constants. Yet, such a constant is in general included in the actual form of the MMSEE, \hat{X}_M , *e.g.*, for a Gaussian channel and a Gaussian prior, \hat{X}_M is a weighted sum of the prior mean, which is a constant, and the data. We can thus estimate the form of the MMSEE only up to an arbitrary additive constant even when the UB approximates the MMSE very well. To fix this constant, we need an additional constraint obeyed by the MMSEE, namely that its mean be the same as the prior mean.

Multi-Parameter Generalization of the MMSE and Upper Bound As is well known, the form (23) of the MMSEE remains valid for the most general definition of the MSE for multivariate parameter and data vectors,

$$\mathcal{E} \stackrel{\text{def}}{=} \mathbb{E}\{[\hat{\underline{X}}(\underline{Y}) - \underline{X}]^T \mathbf{R} [\hat{\underline{X}}(\underline{Y}) - \underline{X}]\}, \quad (31)$$

where \mathbf{R} is a positive-definite, symmetric, real matrix. We need only interpret (23) as being the MMSE estimator for each parameter,

$$\hat{X}_{nM}(\underline{Y}) = \mathbb{E}_{X|Y}(X_n) = \int x_n P(x_n|\underline{Y}) dx_n, \quad n = 1, \dots, N_x, \quad (32)$$

where N_x is the total number of parameters being estimated. Consequently, the upper-bound formula (25) undergoes a simple modification to the form

$$\mathcal{E}_M \leq \mathcal{E}_{UB},$$

where

$$\mathcal{E}_{UB} = \mathbb{E}\{[\delta \hat{\underline{X}}(Y) - \delta \underline{X}]^T \mathbf{R} [\delta \hat{\underline{X}}(\underline{Y}) - \delta \underline{X}]\}. \quad (33)$$

1.5.2 A MAP Estimator Based MMSE Upper Bound

One approach for choosing a good trial estimator is to use a weighted sum of the MAP estimator and the mean value of the prior and to pick the two weights by requiring that the expected value of the estimator, like the true MMSE estimator, be the same as the prior mean and that the MSE computed for this estimator be as small as possible (for the tightest UB). The two requirements fix the weights, thus yielding both an approximate value (in the UB sense) of the MMSE and a good approximation to the true MMSE estimator. Some results of this approach are shown in Fig. 5 for the problem of estimating the center of a Gaussian-shaped source on a pixel line in the presence of Gaussian noise. We have plotted the MMSE, calculated numerically (with difficulty), and the UB obtained by the approach we have just outlined. Other well known bounds, specifically the Ziv-Zakai and Weiss-Weinstein bounds that are lower bounds on MMSE, are also presented on the same plot. The superiority of the UB obtained in our work is evident as it hugs the true MMSE more closely than the two lower bounds as well as a pure MLE based UB, as shown.

1.5.3 A Quasilinear Variational Bound: Piecewise Linearization

A typical issue facing the choice of a good trial estimator is the nonlinear dependence of the data mean on the parameter being estimated. In the 1D localization problem, the nonlinearity is present in the Gaussian dependence of the mean data vector on the center position of the true Gaussian signal, denoted by $\underline{G}(\theta)$, where θ is its center position being estimated here. Correspondingly, a good estimator of the center position cannot depend linearly on the data, making the choice of a good estimator a difficult one. As we have seen, a weighted MAP estimator provides a good choice, but determining the MAP estimator itself may be a highly daunting task requiring extensive nonlinear-optimization based computation.

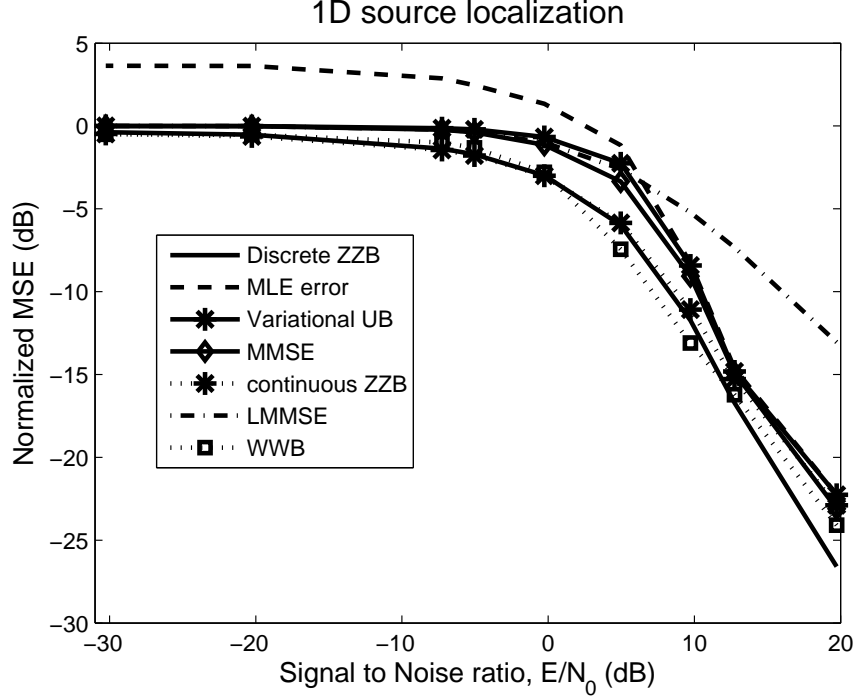


Figure 5: The MMSE and various lower and upper bounds on it for the problem of 1D source localization in the presence of Gaussian additive noise

A good, computationally simple alternative to the MAP approach is to approximate the required estimator piecewise, so it works well for a wide interval of prior values over which the mean data vector depends nonlinearly. Since over a small sub-interval of parameter values the data may be regarded as being approximately linearly dependent on the parameter, a good approximation to the estimator may be had via the following piecewise linearized form:

$$\hat{\theta}(\underline{Y}; \mathbf{A}, \underline{b}) = \sum_{i=1}^{N_\theta} (b_i + \underline{a}_i^T \underline{Y}) \exp[-\|\underline{Y} - \underline{G}(\theta_i)\|^2/w^2], \quad (34)$$

where $\underline{G}(\theta_i)$ is the vector of intensity values that depend on the pixel index via the given Gaussian function evaluated for the center position θ being equal to the mid-point of the i th subinterval of the full θ interval. The use of such Gaussian weight enforces in the above linear sum enforces its piecewise linearity, while allowing for linear variational parameters in terms of the matrix \mathbf{A} of column vectors \underline{a}_i , representing linear gain, and the elements of the vector \underline{b} linear bias, one for each subinterval. In spite of the nonlinearity posed by the data-dependent Gaussian weights, the calculation of the MSE for the estimator $(\hat{\theta})$ is analytically straightforward since its form is identical to the Gaussian form of the conditional PDF of the data vector \underline{Y} , given θ . Indeed, the same analytical expediency can be built into *any* specific form of the conditional data PDF, as long as there is a one-to-one correspondence, however nonlinear, between the mean data vector and the parameter value and the weight factor is chosen to be of the same analytical form as the conditional data PDF.

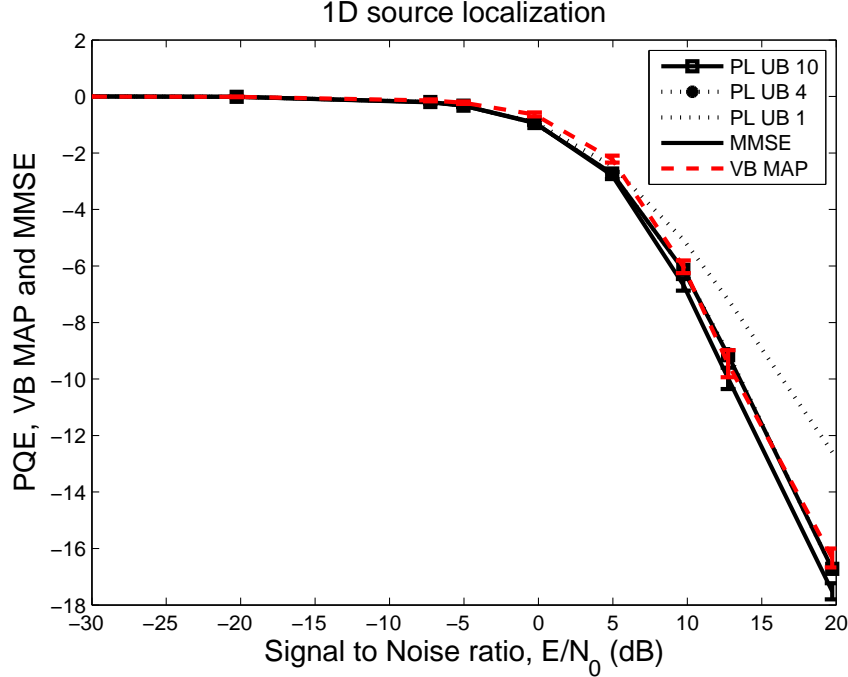


Figure 6: The MMSE and various upper bounds on it for the problem of 1D pulse-center localization from a time series in the presence of Gaussian additive noise

In Fig. 6, we display the results for the numerically exact MMSE and its upper bounds computed by variational MAP and piece-wise linearization approaches covered above, for the problem of estimation of the center of a pulse that is corrupted by additive Gaussian noise. The width of the pulse is $\sqrt{3}$ units, while the prior on the center is distributed uniformly over the range (30,40) (in the same units). The SNR plotted on the x axis is simply the ratio of the total pulse signal energy and the total noise energy, E/N , with the noise energy, N , being the variance of the read noise per time sub-interval, taken to be 0.1 long, times the total number of such sub-intervals, about 700 in all, in the full time series. The MMSE and MAP-based variational bounds were computed for 50 different noise realizations, with corresponding finite but sufficiently error bars on those bounds shown in the plot. Note the excellent accuracy provided by the piece-wise linearized versions of the variational estimator, for $N_\theta = 1, 4$, and 10 subintervals over which the full range (30,40) of the pulse center, θ , is subdivided according to the piece-wise linearization protocol described above. As expected, the agreement of the corresponding bounds with the exact MMSE improves dramatically from 1 to 4 to 10 subdivisions of this range.

Other problems, including 2D point-source localization using a imager with Gaussian PSF and different noise statistics, such as Poisson conditional data treated via a pseudo-Gaussian PDF approximation, have also been treated for our MAP-based and piecewise linearized variational upper bounds. In each case, the upper bounds obtained in these ways have been found to be tight and numerically efficient to compute.

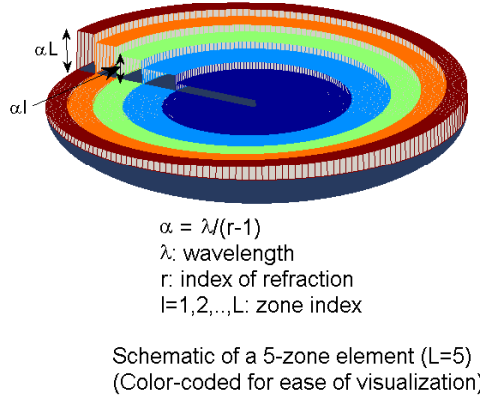


Figure 7: A schematic of the optical element with its spiral phase retardation

1.6 3D Imaging and Source Ranging via a Rotating Point-Spread Function

In a recent work [3], we have proposed and evaluated a novel rotating PSF design by means of wavefront coding. The imaging pupil in this design is subdivided into Fresnel zones, with each zone carrying a radially uniform but azimuthally spiraling phase profile with an integral number of turns in a complete circuit around the pupil center. The number of turns of the spiral phase is taken to increment by 1 between two successive Fresnel zones. For such a pupil phase plate, shown in Fig. 7, the PSF merely rotates with changing defocus of the source point, without spreading significantly, over a considerable range of defocus values. While the PSF itself is not as compact as the in-focus Airy disk PSF obtained with a clear, well-corrected pupil, its non-spreading character lends it a potential to determine the depth distribution of a collection of point sources in a single snapshot. This increased efficiency, with little degradation of sensitivity with defocus, enables it to provide a fast image of a 3D scene of point sources without having to refocus the imager at different focal depths in a sequential manner. Applications to space-borne imagers that provide surveillance of the space environment in the vicinity of a space asset against debris and other potential threats are immediate for this imager.

For such a phase mask in the imaging pupil, the resulting PSF rotates with defocus, largely maintaining its shape and size over a large range of values of the defocus. This is illustrated well in Fig. 8 where we make color-coded surface plots of the PSF for a number of different values of the defocus-induced quadratic phase, ζ , at the edge of the pupil. The top row displays the PSF rotation for the spiral pupil-phase mask described here, while the bottom row presents the corresponding conventional clear-aperture PSFs that exhibit large spreading and loss of sensitivity over the same range of defocus values.

The wavefront-coded imager works in the trade space of transverse and longitudinal reso-

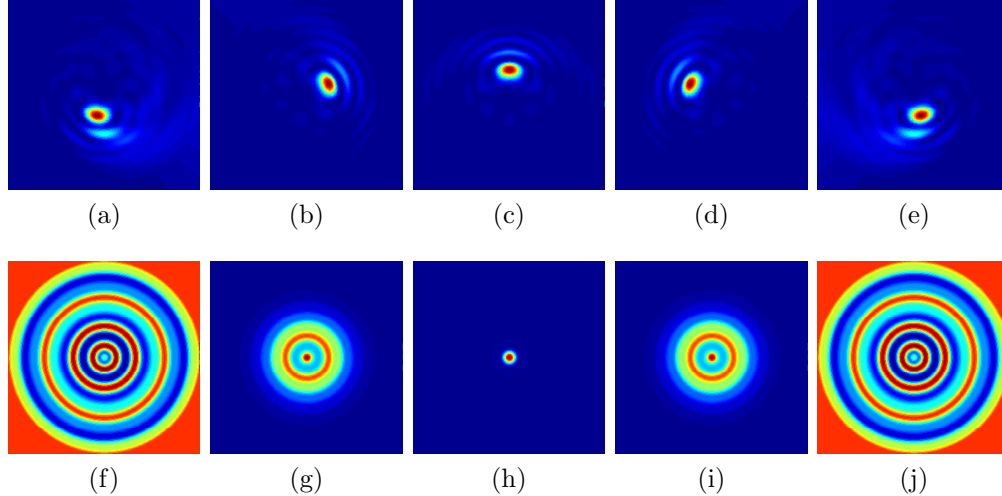


Figure 8: Surface plots of the rotating PSF, with $L = 7$ Fresnel zones (top row). The plots from left to right are for increasing values of defocus, namely -24 , -8 , 0 , 8 , and 24 radians at the pupil edge. The conventional clear-aperture PSF is shown in the bottom row of plots for the same values of defocus.

lutions, and thus provides a fertile setup to explore such tradeoffs in computational imaging. The generalization of this concept to include the vector nature of the electromagnetic field and thus to provide a potential polarimetric imager is currently being investigated. While this work was not a direct result of any task initially proposed under the current grant, its serendipitous discovery has given a new direction and impetus to our work.

1.7 Statistical Bayesian Analysis of 3D Source Super-localization Using a Rotating-PSF Imager

We have analyzed certain statistical upper bounds on the performance of a rotating-PSF-based imager for a complete 3D super-localization and super-resolution of point sources and compared its performance, via these upper bounds, to that of a conventional imager. Two kinds of Bayesian estimators, specifically the mean and mode of the posterior probability density function (PDF), are adopted for our calculations. The first is associated with the minimum mean-squared error (MMSE) and the latter with the minimum probability of error (MPE) in a multi-hypothesis testing (MHT) based Bayesian inference. The two error bounds provide somewhat different quantitative metrics of performance, but are closely related at high SNR [2].

The problem of localizing a point source to sub-diffractive uncertainties in 3D may be phrased in terms of the minimum error in localizing the source to within one of $M_{\perp}^2 \times M_{\parallel}$ possible sub-voxels into which a nominal voxel, corresponding to the diffraction-limited resolution volume, is subdivided uniformly. The integers M_{\perp} and M_{\parallel} represent the transverse and axial localization enhancement factors, respectively. The problem can be posed either as a spatial error bound problem, described by the MMSE metric, or as an MHT problem, described by the MPE metric. The Bayesian prior in each case must be chosen as being

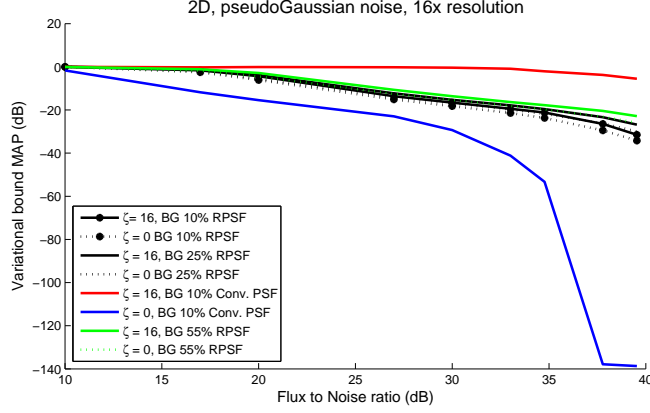


Figure 9: MMSE vs. FNR for conventional and rotating-PSF based imagers for 2D source localization, at different background levels.

uniform over the $M_{\perp}^2 \times M_{\parallel}$ sub-voxels.

Some preliminary results [4,5] for the two approaches under a combination of sensor read noise and signal and background based shot noise sources are presented in Figs. 9-10 below. For the MMSE based description of transverse (2D) source localization, we find that at sufficiently high SNR, defined here as the source flux-to-noise ratio (FNR), the MMSE is reduced well below its zero-SNR value, namely the prior variance. A reduction of the MMSE by a factor M_{\perp}^2 represents an M_{\perp} -fold transverse super-localization, with the associated FNR providing a lower bound on the FNR needed to achieve it. As seen in Fig. 9, the conventional imager at best focus yields a rapid decrease in 2D-localization MMSE with increasing FNR, but its behavior is reversed at large defocus, e.g., at $\zeta = 16$ radians for which the MMSE shows little reduction even at FNR = 40 dB. By contrast, the rotating-PSF imager has a rather robust 2D-localization performance, with all of the MMSE vs. FNR curves closely bunched, over any defocus phase between 0 and 16 radians.

Figure 10 captures similar 2D-localization trends for the two imagers from the MPE perspective. For N pixels of image data, when $N \gg 1$ it is possible to develop an asymptotic analysis of the MPE for an image-based Bayesian MHT problem that involves complimentary error functions [5]. The agreement between the exact and asymptotic MPE values, as the figure shows, is quite good at large FNR.

We have also confirmed a cross-over behavior of the MPE vs. defocus for 2D localization between the two imagers, since the conventional imager has a better performance at the plane of best focus but rapidly degrades with increasing defocus while the rotating-PSF imager has a rather constant performance across a large range of defocus. This behavior is consistent with the fact that with increasing defocus the rotating PSF maintains its size and shape, but the conventional PSF spreads rapidly and thus loses its sensitivity to localize a source in the transverse plane.

Finally, we have also computed the exact and asymptotic values of the MPE for full 3D source super-localization. An interesting competition between transverse and axial (depth) localization enhancement is seen here, with the latter providing the limiting behavior of the MPE in the limit of high FNR. Also, the conventional imager performs poor depth

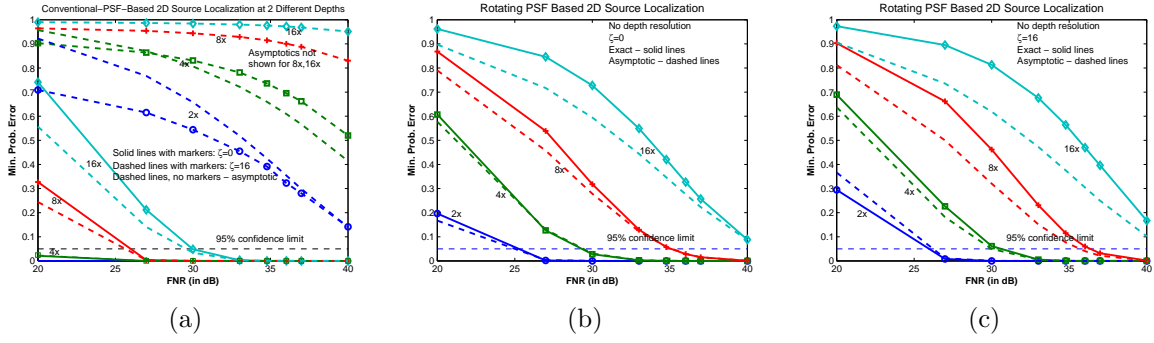


Figure 10: Plots of MPE vs. FNR for the rotating-PSF imager for two values of defocus, (a) $\zeta = 0$; (b) $\zeta = 16$. (c) The same plot for the conventional imager for the same two values of ζ . The asymptotic MPE values are shown by dashed line segments without any marker symbols.

localization at the plane of best focus where it has vanishing first order derivative relative to defocus and thus no first-order sensitivity to depth localization. These and other details of full 3D localization are contained in Ref. [5].

1.7.1 A Bayesian MPE Based Analysis of 2D Point-Source-Pair Superresolution

In a second recently submitted paper [6], a related problem of the optical superresolution (OSR) of a pair of equal-brightness point sources separated spatially by a distance (or angle) smaller than the nominal diffraction-limited resolution spacing (or angle) has been analyzed from the same Bayesian perspective of the MPE. The question was posed as a Bayesian binary-hypothesis testing problem of discriminating between a null hypothesis - that there is a single point source with double the brightness of each point source in the pair - and an alternative hypothesis - that there are indeed two point sources. This problem was studied under the same noise and background conditions under which we studied 3D super-localization discussed in the previous subsection. The correct hypothesis is chosen with little error, determined by the MPE dropping below a lower threshold typically at 5%, equivalent to a 95% statistical confidence level, provided the source brightness exceeds a certain upper threshold that is determined by the smallness of the (sub-diffractive) source separation and background/noise levels. Without going into the details of a rather complex calculation presented in the paper [6], which is based on some asymptotically valid theoretical expressions for the MPE derived in the earlier paper [5], we present only the most important findings of this work.

First, the minimum brightness needed to achieve pair OSR in the signal-dominated regime scales approximately as the fourth power of the inverse source-pair spacing, but the scaling is modified from its quartic behavior by logarithmic corrections that have not been inferred by any of the previous analyses of this problem. Second, in the background-dominated regime, the same scaling law is moderated to a pure quadratic form, with a slow transition from the logarithmically modified quartic power law dependence as the signal strength increases

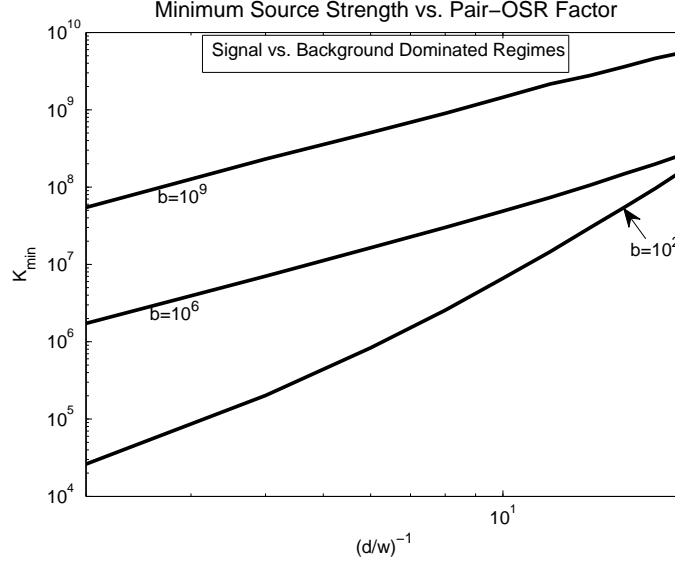


Figure 11: Log-log plots of the minimum source strength, K_{min} , vs. the OSR ratio, w/d , for the three different background levels.

relative to the background level. These scaling laws are seen in Fig. 11 where we plot the minimum source strength, K_{min} (in photon number units), versus the inverse ratio of the pair spacing, d , to the diffractive resolution spacing, w , on a log-log plot. The slow change of the slope of the $\log_{10} K_{min}$ vs. $\log_{10}(d/w)$ from 4 to 2 with increasing background levels is quite evident in this plot.

More details of this work may be found in Ref. [6] where we present detailed derivations of the various scaling laws under varying conditions of signal to background ratios. While the pair OSR problem was analyzed here in the plane of best focus for a Gaussian PSF based imager, the analysis can be readily generalized to other PSFs and to full 3D pair OSR as well. This is currently being studied by the UNM group.

2 Publications Citing Grant Funding Support

1. Q. Zhang, R. J. Plemmons, D. Kittle, D. Brady, and S. Prasad, "Joint Segmentation and Reconstruction of Hyperspectral Data with Compressed Measurements," *Appl. Opt.* **50**, Iss. 22, pp. 4417-4435 (2011).
2. S. Prasad, "New error bounds for M-testing and estimation of source location with subdiffractive error," *J. Opt. Soc. Am. A* **29**, 354-366 (2012).
3. S. Prasad, "Rotating point spread function via pupil-phase engineering," *Opt. Lett.*, vol. 38, pp. 585-587 (2013).
4. S. Narravula, R. Kumar, and S. Prasad, in preparation.

5. S. Prasad, "Asymptotics of Bayesian error probability and rotating-PSF-based source super-localization in three dimensions," submitted to Opt. Express (2014); published as arXiv:1403.4897 [physics.optics] (19 March 2014).
6. S. Prasad, "Asymptotics of Bayesian error probability and 2D pair superresolution," submitted to Opt. Express (2014); published as arXiv:1403.4919 [physics.optics] (19 March 2014).
7. Zhang, Q., Plemmons, R.J., Kittle, D., Brady, D., and Prasad, S., "Reconstructing and Segmenting Hyperspectral Images from Compressed Measurements," IEEE Conference on Remote Sensing, Lisbon, Portugal (2011). Available at <http://www.wfu.edu/~plemmons/papers/Wsegrec.pdf>
8. Kittle, D., Zhang, Q., Plemmons, R.J., Brady, D., and Prasad, S., "Joint Segmentation and Reconstruction of Coded Aperture Hyperspectral Data," *Computational Optical Sensing and Imaging (COSI)* Topical Meeting of the Optical Society of America, Toronto, Canada (July 2011). Abstract available at <http://www.opticsinfobase.org/abstract.cfm?URI=COSI-2011-CMD1>
9. Prasad, S., and Narravula, S., "Applications of Shannon information and statistical estimation theory to inverse problems in imaging," *Signal Recovery and Synthesis (SRS)* Topical Meeting of the Optical Society of America, Toronto, Canada (July 2011). Abstract available at <http://www.opticsinfobase.org/abstract.cfm?URI=SRS-2011-SMC1>
10. Zhang, Q., Plemmons, R.J., Kittle, D., Brady, D., and Prasad, S., "Joint Segmentation and Reconstruction of Hyperspectral Data from a Single Snapshot," Proc. SPIE Defense, Security and Sensing, Orlando, FL. Proc. of SPIE, vol. 8048 (2011). Limited availability at <http://spie.org/x648.html?productid=881777>
11. Prasad, S. and Zhang, Q., "Exploiting Spectral Correlations for Segmentation and Shape Determination from Hyperspectral Datacubes of Rotating Satellites," Advanced Maui Optical and Space Surveillance (AMOS) Technical Conference (Sep 2010). Available at <http://www.amostech.com/TechnicalPapers/2010.cfm>
12. Li, F., Ng, M., Plemmons, R.J., Prasad, S., and Zhang, Q., "Coupled Segmentation and Denoising/Deblurring Models for Hyperspectral Material Identification, Proc. SPIE Defense, Security and Sensing, vol. 7701, paper no. 7701-2 (2010).
13. S. Prasad and D. Hope, "Information theoretic characterizations of compressive-sensing-based space object identification," Proc. of SPIE, vol. 7800, pp. 78000B-1:11 (2010).
14. Prasad, S., and Luo, X., "Support-assisted optical superresolution of low-resolution image sequences: The one-dimensional problem," Opt. Express, vol. 17, pp. 23213-23233 (2009).
15. Prasad, S., and Luo, X., "An information theoretic analysis of support assisted optical superresolution in one and two dimensions," Paper CTuC3 presented at the Computational Optical Sensing and Imaging Conference, San Jose, CA, Oct. 10-12, 2009. Available at <http://www.opticsinfobase.org/abstract.cfm?uri=COSI-2009-CTuC3>

16. Prasad, S., and Luo, X., "Support-based digital and optical superresolution in one and two dimensions," Proceedings of the 2009 AMOS Technical Conference, Maui, HI, Sep 1-4, 2009. Available at <http://www.amostech.com/TechnicalPapers/2009.cfm>
17. Hope, D., and Prasad, S., "A statistical information based analysis of a compressive imaging system," Proceedings of the 2009 AMOS Technical Conference, Maui, HI, Sep 1-4, 2009. Available at <http://www.amostech.com/TechnicalPapers/2009.cfm>
18. S. Prasad, Q. Zhang, R. Plemmons, and D. Brady, "Statistical performance bounds for coded-aperture compressive spectral-polarimetric imaging," *Computational Optical Sensing and Imaging (COSI)* Topical Meeting of the Optical Society of America, Monterey, CA (24-27 June 2012). Abstract available at <http://www.opticsinfobase.org/abstract.cfm?URI=COSI-2012-CTu3B.1>
19. Rakesh Kumar and S. Prasad, "PSF Rotation with Changing Defocus and Applications to 3D Imaging for Space Situational Awareness," Proceedings of the 2013 AMOS Technical Conference, Maui, HI, Sep 10-13, 2013. Paper (9 pages) available at <http://www.amostech.com/TechnicalPapers/2013.cfm>
20. S. Prasad, Q. Zhang, and R. Plemmons, "Shape, Pose, and Material Recovery of Solar-Illuminated Surfaces from Compressive Spectral-Polarimetric Image Data," Proceedings of the 2013 AMOS Technical Conference, Maui, HI, Sep 10-13, 2013. Available (8 pages) at <http://www.amostech.com/TechnicalPapers/2013.cfm>

3 Invited Presentations

1. S. Prasad, "Angular Momentum, Rotating PSF, and 3D Source Localization," an invited seminar presented at the Institute of Quantum Science and Engineering (IQSE), Texas A&M Univ., College Station, TX, Jan 17, 2014.
2. S. Prasad, "Cooperative Radiation and Scattering by a Resonant Medium," an invited presentation at the 43rd Physics of Quantum Electronics (PQE) Winter Colloquium Snowbird, UT, Jan 6-10, 2013.
3. S. Prasad, "Imaging via Information, Coding, and Compression," an invited colloquium at UNM Physics and Astronomy, Nov 30, 2012.
4. S. Prasad, "Statistical performance bounds for coded-aperture compressive spectral-polarimetric imaging," invited presentation at the *Computational Optical Sensing and Imaging (COSI)* Topical Meeting of the Optical Society of America, Monterey, CA, 26 June 2012.
5. S. Prasad, "A Physicist's Perspective on Modern Imaging Systems," an invited lecture given in the Dept of Appl. Physics at the Benaras Hindu University (BHU), India, November 8, 2011.

6. S. Prasad, “Applications of Shannon information and statistical estimation theory to inverse problems in imaging,” invited presentation at the *Signal Recovery and Synthesis* Topical Meeting of the Optical Society of America, Toronto, CA (July 11, 2011).

4 Other Presentations

1. R. Kumar, S. Narravula, and S. Prasad, “PSF Rotation with defocus and applications to 3D localization,” a poster presented at the 2014 Conference on Quantitative BioImaging in Albuquerque, NM, January 9-11 (2014).
2. S. Prasad, “PSF Rotation with Changing Defocus and Applications to 3D Imaging for Space Situational Awareness,” presented at the 2013 AMOS Technical Conference, Maui, HI, Sep 10-13, 2013. Paper (9 pages) available at <http://www.amostech.com/TechnicalPapers/2013.cfm>
3. S. Prasad, Q. Zhang, and R. Plemmons, “Shape, Pose, and Material Recovery of Solar-Illuminated Surfaces from Compressive Spectral-Polarimetric Image Data,” poster presented at the 2013 AMOS Technical Conference, Maui, HI, Sep 10-13, 2013. Paper (8 pages) available at <http://www.amostech.com/TechnicalPapers/2013.cfm>
4. S. Prasad, Q. Zhang, and R. Plemmons, “Exploiting Spectral Correlations for Segmentation and Shape Determination from Hyperspectral Datacubes of Rotating Satellites,” 2010 AMOS Technical Conference, Maui, HI, Sep 14-17, 2010.
5. S. Prasad, “Information Theoretic Characterizations of Compressive Sensing Based Space Object Identification,” SPIE’s *Image Reconstruction from Incomplete Data VI* (IRID) Symposium (August 2010).

5 Patents

1. S. Prasad, “Rotating Point-Spread Function (PSF) Design for Three-Dimensional Imaging,” filed with the US Patent and Trademark Office, Serial No. 14/202,915 (10 March 2014).